Bioactive Materials 34 (2024) 269–281

Contents lists available at ScienceDirect

Bioactive Materials

journal homepage: www.keaipublishing.com/en/journals/bioactive-materials

A tough, antibacterial and antioxidant hydrogel dressing accelerates wound healing and suppresses hypertrophic scar formation in infected wounds

Xiaoqing Liu [a,1], Yiming Sun [b,1], Jie Wang [a], Yongyuan Kang [a], Zhaolong Wang [a], Wangbei Cao [a], Juan Ye [b,**], Changyou Gao [a,c,d,*]

[a] MOE Key Laboratory of Macromolecular Synthesis and Functionalization, Department of Polymer Science and Engineering, Zhejiang University, Hangzhou, 310058, China
[b] Eye Center, The Second Affiliated Hospital of Zhejiang University, School of Medicine, Hangzhou, 310009, China
[c] Center for Healthcare Materials, Shaoxing Institute, Zhejiang University, Shaoxing, 312099, China
[d] Shanxi-Zheda Institute of Advanced Materials and Chemical Engineering, Taiyuan, 030000, China

ARTICLE INFO

Keywords:
Hydrogel dressing
Hypertrophic scars
Wound healing
Bacterial infection
ROS-scavenging

ABSTRACT

Wound management is an important issue that places enormous pressure on the physical and mental health of patients, especially in cases of infection, where the increased inflammatory response could lead to severe hypertrophic scars (HSs). In this study, a hydrogel dressing was developed by combining the high strength and toughness, swelling resistance, antibacterial and antioxidant capabilities. The hydrogel matrix was composed of a double network of polyvinyl alcohol (PVA) and agarose with excellent mechanical properties. Hyperbranched polylysine (HBPL), a highly effective antibacterial cationic polymer, and tannic acid (TA), a strong antioxidant molecule, were added to the hydrogel as functional components. Examination of antibacterial and antioxidant properties of the hydrogel confirmed the full play of the efficacy of HBPL and TA. In the *in vivo* studies of methicillin-resistant *Staphylococcus aureus* (MRSA) infection, the hydrogel had shown obvious promotion of wound healing, and more profoundly, significant suppression of scar formation. Due to the common raw materials and simple preparation methods, this hydrogel can be mass produced and used for accelerating wound healing while preventing HSs in infected wounds.

1. Introduction

Skin is an organ directly contacting with the outside world, which is highly vulnerable to injury. Hypertrophic scars (HSs) often appear after deep skin injuries such as trauma, burns and surgery. The itching, pain, and other discomfort caused by HSs as well as appearance issues such as bulge, flushing, and crispation have resulted in great inconvenience to about 100 million patients' lives from both functional and aesthetic aspects in developed countries [1]. The generation and development of HSs are closely related to the wound healing process [2], which typically involves a series of continuous stages: hemostasis, inflammation, proliferation, and remodeling [3,4]. When these stages proceed abnormally, for example, inflammatory stage persists or wound healing is delayed, pathological scars such as HSs will occur [5,6].

Essentially, the HSs are an inflammatory disease of the reticular dermis, characterized by prolonged inflammatory response, excessive angiogenesis and accumulation of myofibroblasts and collagen. Various stimuli may promote inflammation, especially oxidative stress [7]. Another typical reason is bacterial infection, the most common and unavoidable challenge in wound healing [8]. If not treated promptly, the wounds are easily colonized by pathogens, ultimately leading to severe scars [9]. Bacterial resistance is a serious issue that follows [10]. One prevalent microbial strain in infected wound patients is Methicillin resistant *Staphylococcus aureus* (MRSA), which is related to nearly 11000 deaths in the United States each year [11]. Currently the available antibiotics for wound healing include tetracyclines, neomycin, quinolones,

Peer review under responsibility of KeAi Communications Co., Ltd.
* Corresponding author. MOE Key Laboratory of Macromolecular Synthesis and Functionalization, Department of Polymer Science and Engineering, Zhejiang University, Hangzhou, 310058, China.
** Corresponding author.
E-mail addresses: yejuan@zju.edu.cn (J. Ye), cygao@zju.edu.cn (C. Gao).
[1] Xiaoqing Liu and Yiming Sun contributed equally to this work.

https://doi.org/10.1016/j.bioactmat.2023.12.019
Received 29 October 2023; Received in revised form 15 December 2023; Accepted 21 December 2023

and the like [12]. However, due to the induction of drug resistance, safety concerns at large doses and declined development speed and investment, the antimicrobial strategies for non-antibiotic treatment have become a topic of great concern [13].

Clinical strategies for HSs can be divided into preventing scar formation and treating formed scars. Correspondingly, there are methods available in clinic, such as tension reduction therapy and surgical therapy [14], although they do not work satisfactorily enough. Some antibacterial or anti-proliferative functional wound dressings exhibited HSs generation inhibition [15–17]. However, limited to animal models (rats or mice), these researches on anti-scar effects are not comprehensive and clear enough. Based on rabbit ear hypertrophic scar model, there are many meaningful researches reported in recent years. Guided by the idea of preventing of scar formation, the scar could be suppressed by various ways, such as inhibiting TGF-β or *Engrailed-1* [18–20], reducing inflammatory reactions [21], and regulating vascular proliferation and collagen deposition [22]. Also, mechanical regulation or mediated iron death through microneedles has achieved promising results in the treatment of HSs [23,24]. Yet these studies have ignored or intentionally controlled the potential impacts of bacterial infections. Considering the multiple and widespread nature of bacterial infections, it is necessary to clarify the prevention and treatment of scars in infection situations.

Hyperbranched polylysine (HBPL) is a novel and highly efficient antibacterial polymer in the post antibiotic era, obtained through the polymerization of L-lysine [25]. Its antibacterial principle is similar to that of antimicrobial peptides: a large number of amino groups in the hyperbranched structure endow HBPL with the positive electric property, which can bind to bacterial cell membranes through electrostatic action, and then destroy the cell membrane and kill bacteria [26]. The broad-spectrum, high-efficient antibacterial property and biosecurity of HBPL, with its application in dental implants and wound dressings, have already been confirmed [27–29]. Tannic acid (TA) is a natural-source polyphenol compound with excellent antioxidant function [30]. Recently, TA has set off a wave of enthusiasm in the field of hydrogel wound dressings [31–33]. Furthermore, hydrogels with mechanical properties matching with the skin are emphasized as the best choice for wound dressings [34]. Polyvinyl alcohol (PVA) is one of the most commonly used hydrogel raw materials with excellent compatibility and processability, and can be prepared by various methods to obtain strong and tough hydrogels [35–37]. Building a double network structure is a universal method of strengthening and toughening [38] with simple steps, low equipment requirements, and convenience for expanding production.

Herein, aiming at controlling the inflammation by reducing bacterial infection and oxidative stress, we propose a tough hydrogel dressing to promote healing of infected wounds and control scar formation. The double network of PVA and agarose can provide the main support for the excellent mechanical properties of the hydrogel, and the loading of HBPL and TA would endow the hydrogel with anti-bacterial and anti-oxidation abilities (Scheme 1). The hydrogel's mechanical property, antioxidant and antibacterial capacities as well as its biocompatibility will be verified. Importantly, the *in vivo* anti-scar effect of the hydrogel will be explored through wound healing and hypertrophic scar models under MRSA infection *in vivo*.

2. Materials and methods

2.1. Materials

PVA1799, agarose, 5(6)-tetramethyl rhodamine isothiocyanate (TRITC), 2,2-di(4-*tert*-octylphenyl)-1-picryl-hydrazyl (DPPH) and 3,3′,5,5′-tetramethylbenzidine (TMB) were purchased from Aladdin Biochemical Technology Co., Ltd. (Shanghai, China). Tannic acid (TA), ammonium iron citrate, $FeSO_4$ and KI were purchased form Macklin Chemical Co., Ltd. (Shanghai, China). Hydrogen peroxide (30 %) and ammonium hydroxide were purchased from Sinopharm chemical reagent Co., Ltd. (Beijing, China). Cell Counting Kit-8 (CCK-8) was purchased from Beyotime Biotech Inc. (Shanghai, China). Dulbecco's modified Eagle's medium (DMEM) (containing 100 μg/mL streptomycin and 100 U/mL penicillin) and fetal bovine serum (FBS) were purchased from Thermo Fisher Scientific Inc. (Massachusetts, USA). Superoxide anion scavenging capacity assay kit and anticoagulated sheep blood were purchased from Beijing Solarbio Science & Technology Co., Ltd. (Beijing, China). All enzyme-linked immunosorbent assay (ELISA) kits were purchased from Boster Biological Technology Co. Ltd. (California, USA). The antibody (ab7817) of α-smooth muscle actin (α-SMA) was purchased from Abcam plc. (Cambridge, UK).

2.2. Preparation and properties of hydrogels

2.2.1. Hydrogel preparation

Five types of hydrogel dressings were prepared (Table 1). The HBPL synthesized according to our previous work [39] was used directly.

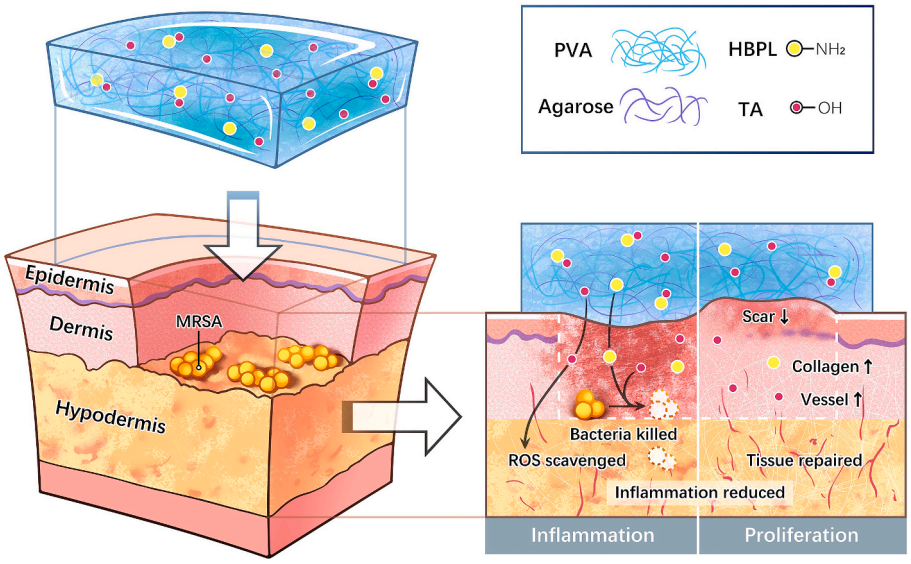

Scheme 1. Schematic illustration of the antibacterial and antioxidant hydrogel dressing for accelerating the infected wounds healing and reducing the hypertrophic scar formation.

Table 1
Abbreviations and components of hydrogels prepared in this study.

Abbreviations	PVA1799 (wt%)	Agarose (wt%)	HBPL (wt%)	Tannic acid (wt%)	Water (wt%)
P	20	0	0	0	80
PA	20	2	0	0	78
PAT	20	2	0	0.8	77.2
PAH	20	2	1	0	77
PAHT	20	2	1	0.8	76.2

Taking the PAHT hydrogel as an example for the hydrogel preparation, 20 wt% PVA1799 and 2 wt% agarose were dissolved in 76.2 wt% water under mechanical agitation at 110 °C. After the solution was cooled to 90 °C, 1 wt% HBPL and 0.8 wt% TA were added, whose pH value was adjusted to 6. After complete dissolution, the solution was casted into a mold, and cooled to room temperature. It was then frozen at −20 °C for 4 h and thawed at room temperature for 1 h. This process was repeated for 3 times. The other hydrogels were prepared with different components following the similar processes.

2.2.2. Mechanical test

The mechanical properties of hydrogels were tested by tensile and compression experiments via a universal material testing machine (5543A, Instron, USA). For the tensile experiments, the rectangular samples with a dimension of 10 mm in width, 60 mm in length and 1.5 mm in thickness were prepared. The stretching rate was set as 20 mm/min. For the compression experiments, the hydrogels were prepared as cylinders with 5 mm in height and 7 mm in diameter. The compression rate was set as 2 mm/min with a strain range of 0–70 %. The slopes of the lines in the strain range of 10–30 % and 10–20 % in the stress-strain curves were respectively used to calculate the tensile and compression elastic moduli. Additionally, in the strain ranges of 0–100 % and 0–50 %, the tensile and compression tests were carried out on the PAHT hydrogel for 20 cycles, respectively.

2.2.3. Measurement of moisturizing properties and swelling ratio

0.2 g hydrogel was placed in an open Petri dish in direct contact with air at 70 % relative humidity and room temperature. The hydrogel mass was weighed at selected time points. The residual mass was calculated as follows:

$$\text{Residual mass } (\%) = \frac{m_t}{m_0} \times 100\% \tag{1}$$

50 mg hydrogel was soaked in 5 mL water at 37 °C, which was taken out at selected time points. The surface water was wiped off before weighing. The swelling ratio was calculated by the following formula:

$$\text{Swelling ratio } (\%) = \frac{m_t - m_0}{m_0} \times 100\% \tag{2}$$

In formula (1) and (2), m_0 and m_t represent the initial weight and the weight at t time, respectively.

2.2.4. Release of HBPL and TA

The release of HBPL from the hydrogels was measured through a fluorescent method. HBPL was fluorescently labeled as follows. After 0.5 g HBPL was dissolved in 20 mL water with pH adjusted to 8.5, 1 mg TRITC dissolved in 2 mL DMSO was slowly added under stirring. The reaction was carried out in dark for 24 h. A dialysis bag with a cut off molecular weight of 500 Da was used to dialyze the product in dark until there was no fluorescence in the buffer. The TRITC-labeled HBPL was obtained after lyophilization. The labeled HBPL was used to prepare the hydrogel in dark as described in Section 2.2.1. Subsequently, 0.5 g hydrogel containing the fluorescently labeled HBPL was immersed in 5 mL water. 200 μL solution was taken out at selected time points, whose fluorescence intensity was measured by a microplate reader (Infinite 200 Pro, Tecan, Switzerland) with excitation and emission wavelengths of 550 nm and 600 nm, respectively. A standard curve was constructed to calculate the HBPL concentration at the same conditions. After each sampling, 200 μL water was added to the solution to maintain the volume constant. Attention should be paid to avoid light throughout the whole process.

The TA release from the hydrogels was similarly studied. After 0.5 g hydrogel was incubated in 5 mL water containing 0.5 mg/mL $NaHSO_3$, 100 μL supernatant was taken out at selected time points, which was mixed with 500 μL water and 100 μL 3.5 mg/mL ferric ammonium citrate solution. It was further mixed with 100 μL 8 mg/mL ammonia solution. After incubation for 10 min, the absorbance at 525 nm was measured by a microplate reader. The TA concentration was calculated by referring to a standard curve constructed at the same conditions. After each sampling, 100 μL water was added to the hydrogel-containing solution.

The cumulative release ratio of HBPL and TA was calculated by the following formula:

$$\text{Cumulative release ratio } (\%) = \frac{\sum_{i=1}^{t-1} c_i v + c_t v_0}{m_0} \times 100\% \tag{3}$$

Where c_i and c_t represent the concentrations of HBPL or TA in the solution measured at i and t time, v and v_0 represent the volumes of solution taken out for each time and the initial volume of solution, respectively, and m_0 is the total mass of HBPL or TA contained in the hydrogel sample.

2.3. Measurement of antioxidant ability

The antioxidant capacity of hydrogels was characterized by testing their ability to scavenge DPPH, ·OH, $\cdot O_2^-$, and H_2O_2 [29]. For the DPPH experiment, 50 mg hydrogel was immersed in 1 mL of 200 μL DPPH ethanol solution and reacted at 37 °C for 1 h. The supernatant was taken to measure the absorbance at 517 nm. For the ·OH experiment, 25 mg hydrogel was immersed in 1 mL 1 mM ·OH solution (500 μL 2 mM H_2O_2 + 500 μL 2 mM $FeSO_4$) and reacted at 37 °C for 30 min, and then 100 μL supernatant was taken out and mixed with 100 μL 10 mM TMB DMSO solution. The mixed solution was allowed to stand for 10 min before the absorbance at 650 nm was measured. The $\cdot O_2^-$ experiment was conducted according to the kit instructions. Briefly, after $\cdot O_2^-$ was generated by AP-TEMED system, 150 mg hydrogel was added to react with $\cdot O_2^-$ for 40 min, then hydroxylamine hydrochloride, 4-aminobenzesulfonic acid and α-naphthylamine were added to react with the rest $\cdot O_2^-$ and subsequently the absorbance at 530 nm was measured. For the H_2O_2 experiment, 200 mg hydrogel was immersed in 1 mL 0.8 mM H_2O_2 solution in 37 °C for 1.5 h, and then 150 μL supernatant was mixed with 150 μL 1 M KI. The absorbance at 350 nm was measured after incubation for 5 min. The solvents were used as blank groups.

The scavenging ratio of DPPH, ·OH, $\cdot O_2^-$ and H_2O_2 was calculated as follows:

$$\text{Scavenging ratio } (\%) = \left(1 - \frac{OD_{gel} - OD_{blank}}{OD_{control} - OD_{blank}}\right) \times 100\% \tag{4}$$

2.4. Antibacterial activity test in vitro

The antibacterial activity of hydrogels was tested by a surface contact method [27]. A circular hydrogel sample with a diameter of 8 mm was prepared, which was irradiated by ultraviolet light for 0.5 h on both sides, and then placed in a 48-well plate. After 5 μL 10^7 CFU/mL bacterial solution was added on the hydrogel surface, the plate was placed in an incubator at 37 °C. After 12 h, the hydrogel was removed, and placed in 1 mL phosphate buffered saline (PBS). The bacteria attached to the surface were washed off by ultrasonication for 5 min. After the bacterial suspension was diluted 100 times, 50 μL solution was coated on LB solid medium, which was then cultured in an incubator at 37 °C for

12–24 h. The plate was photographed to calculate the number of colonies. With the PA group as the control, the antibacterial rate was calculated as follows:

$$\text{Antibacterial rate } (\%) = \left(1 - \frac{Colony\ count_{gel}}{Colony\ count_{PA}}\right) \times 100\% \quad (5)$$

2.5. Cytotoxicity and hemolysis tests

The toxicity of the hydrogels to L929 cells was tested by CCK-8 assay. 90 % DMEM high-sugar medium and 10 % FBS were used. The hydrogel was placed in a serum-free medium at the concentration of 20 mg/mL, and incubated in carbon dioxide incubator at 37 °C for 24 h. After removing the hydrogel, the bacteria, if any, were filtered out, and FBS was added. In 96-well plates, 8000 cells per well were incubated in a carbon dioxide incubator at 37 °C for 24 h. Then the medium was replaced with the hydrogel extract, followed by additional culture medium for another 24 h. The medium was then replaced with the complete medium containing 10 % CCK-8, and the supernatant was taken to test the absorbance at 450 nm after culture for 2 h. The complete medium and cells treated with the complete medium were used as blank group and control group, respectively.

Anticoagulant sheep blood was used to test the hemolysis of hydrogels. The sheep blood was diluted with PBS according to the volume ratio of 1:6. 50 mg hydrogel was placed in 500 μL diluted sheep blood, incubated at 37 °C for 1 h, and then centrifuged at 1000 rpm for 5 min. The supernatant was taken to measure the absorbance at 540 nm. PBS and sheep blood diluted with water were used as blank group and control group, respectively.

The cell viability or hemolysis ratio was calculated as follows:

$$\text{Scavenging ratio } (\%) = \frac{OD_{gel} - OD_{blank}}{OD_{control} - OD_{blank}} \times 100\% \quad (6)$$

2.6. MRSA-infected rat full skin defect model in vivo

The rat experiments were approved by the Experimental Animal Ethics Committee of Hangzhou Medical College following the Institutional Guidelines (ZJCLA-IACUC-20010294). Four-week-old female SD rats (Sprague−Dawley rats) weighing about 200 g were used in the infected wound healing experiment. After the rats were anesthetized by inhalation of 3 % isoflurane, their back hair was removed with a shaver and hair removal cream. Four round full-layer defect wounds with a diameter of 10 mm in each were made with a skin biopsy device. 40 μL 10^8 CFU/mL MRSA bacterial solution was injected into each wound. The hydrogel dressing was applied to the wound and fixed with 3 M Tegaderm Film (3 M Health Care, USA). Five groups were set: Ctrl, PA, PAT, PAH, and PAHT. The Ctrl group was not received any therapeutic measure. The hydrogel dressings were changed every 3 d, and the wounds were photographed. The area of wound was measured using Image J, and the wound closure was calculated by the following formula:

$$\text{Wound closure } (\%) = \left(1 - \frac{Wound\ area_t}{Wound\ area_0}\right) \times 100\% \quad (7)$$

where the $Wound\ area_t$ and $Wound\ area_0$ represent the data on day t and day 0, respectively.

The wound tissues were collected on day 3 and day 6, then ground for Elisa test and *in vivo* antibacterial performance test, respectively. The harvested wound tissues on day 6 and day 12 were fixed with paraformaldehyde for H&E staining, Masson staining and CD31 immunohistochemical staining, following the standard protocols [25]. The blood vessel density in CD31 staining was calculated [25].

2.7. MRSA-infected rabbit ear hyperplastic scar model in vivo

2.7.1. Scar formation analysis

The rabbit experiments were approved by the Experimental Animal Ethics Committee of Hangzhou Medical College following the Institutional Guidelines (ZJCLA-IACUC-20010315). Adult male New Zealand white rabbits (2.5–3 kg) were used for the hyperplastic scar model with MRSA infection. After the rabbits were anesthetized by intravenous injection of dexmedetomidine (0.05 mg/kg), chlorpromazine (2.5 mg/kg) and lidocaine (1 mg/kg), four circular wounds with a diameter of 10 mm and an interval of more than 10 mm were made on the ventral side of each ear using a corneal trephine. The perichondrium was carefully removed with a periosteal separator while avoiding cartilage damage. The injection of bacterial solution and material grouping were the same as those in the rat model. The dressings were changed every 3 d until the wound healed completely (4 w). Photographs were taken every week. The scar tissues were collected after 8 w, and fixed with paraformaldehyde or preserved at −80 °C.

H&E staining, Masson staining, Sirius red staining (polarized light observation), and α-SMA immunofluorescence staining were used for histological observation and examination [20]. The H&E and Masson staining photos were processed with Image J to calculate the thickness and scar elevation index (SEI), and collagen volume fraction (CVF), respectively. The SEI calculation is shown in Fig. 5A, where α+β represents the scar tissue area and β represents the normal skin area. CVF was calculated as follows:

$$\text{CVF } (\%) = \frac{Bule\ area}{Tissue\ area} \times 100\% \quad (8)$$

2.7.2. RNA sequencing analysis

The scar tissues of rabbit ears at the 8th w were collected and washed with saline, and stored at −80 °C before sequencing. Eukaryotic mRNA sequencing was based on Illumina Novaseq 6000 sequencing platform. Illumina TruseqTM RNA sample prep Kit was used to construct the library. The operation process was as follows: total RNA extraction, mRNA enrichment, mRNA fragmentation, cDNA inversion synthesis, adaptor connection, and Illumina sequencing.

2.8. Statistical analysis

All results are expressed as the mean ± standard deviation (SD). The statistical significance between the samples was analyzed by the *t*-test (two groups) or one-way analysis of variance (ANOVA, multiple groups). GraphPad Prism software was utilized for data analyses. The statistically significant difference between groups was expressed as * $P < 0.05$, ** $P < 0.01$ and *** $P < 0.001$.

3. Results and discussion

3.1. Preparation and characterization of hydrogel

To prepare the hydrogel with robust mechanical strength, a double network hydrogel was prepared from PVA and agarose [25]. The PVA was crystallized by freeze-thawing cycles to form the primary physical crosslinking network, and the agarose formed the second physical crosslinking network through hydrogen bonding. The antibacterial and antioxidant functions were achieved by directly mixing HBPL and TA into the bulk hydrogel solution before gelation.

In order to maintain the well contact with human skin and facilitate daily operation, a qualified hydrogel dressing should possess robust enough mechanical properties [40]. Fig. 1A and B shows that the tensile resistance of all double network hydrogels including PA was significantly improved, compared with that of the PVA hydrogel (P). The addition of HBPL (PAH) achieved a larger degree of enhancement, while TA (PAT) had less effect. When both HBPL and TA were present (PAHT),

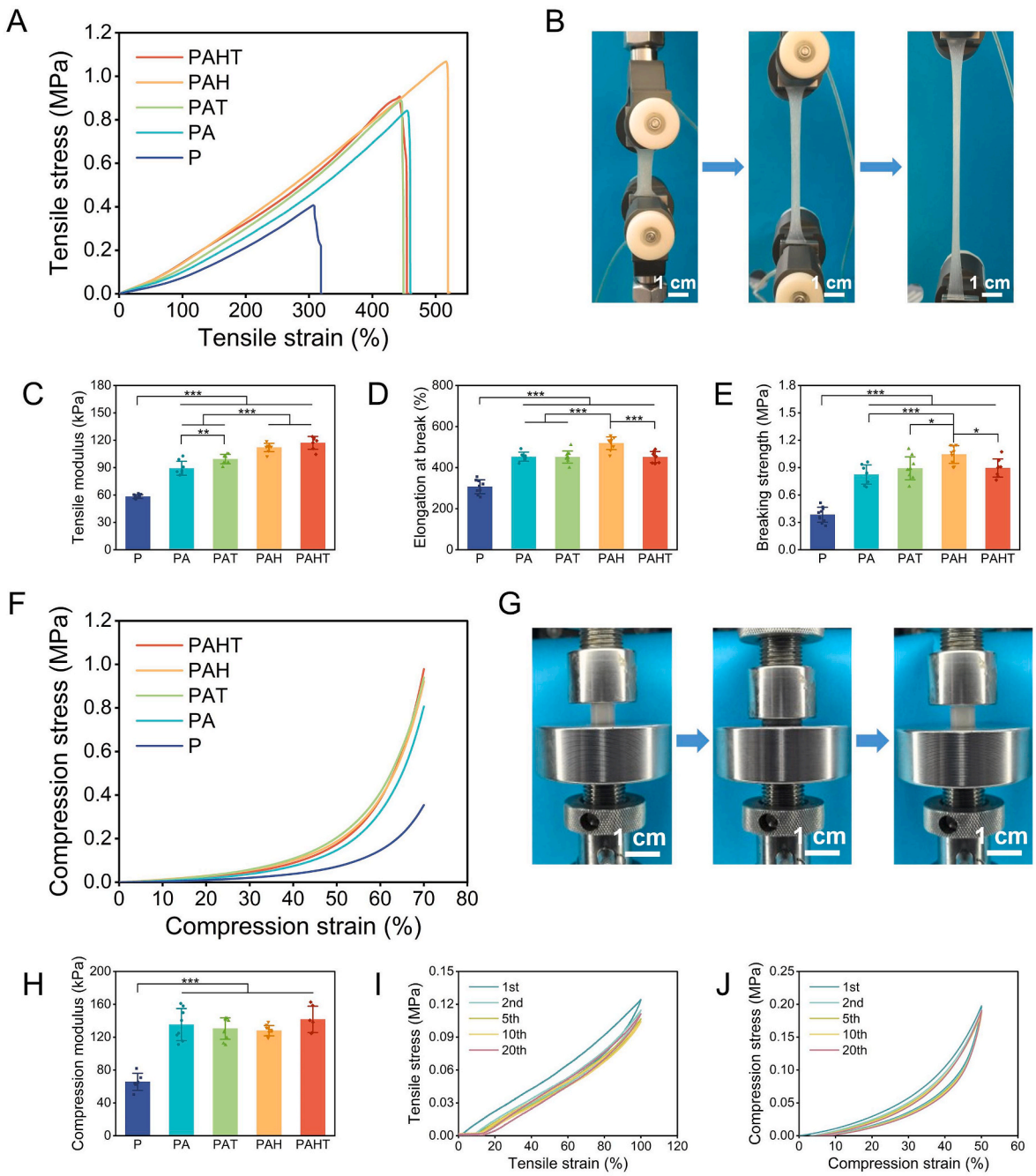

Fig. 1. Mechanical properties of hydrogels. (A) Tensile stress-strain curve of hydrogels with different components. (B) Photos of tensile test of PAHT hydrogel. (C) Tensile modulus, (D) elongation at break, and (E) breaking strength of different hydrogels. (F) Compression stress-strain curves of hydrogels with different components. (G) Photos of compression test of PAHT hydrogel. (H) Compression modulus of different hydrogels. Cyclic tensile (I) and compression (J) curves of PAHT hydrogel. n = 6, *P < 0.05, **P < 0.01 and ***P < 0.001.

the tensile modulus was largest, whereas the elongation at break and breaking strength were decreased slightly (Fig. 1C–E), indicating that their enhancement effect seems to have an antagonistic effect. Nevertheless, the mechanical properties of PAHT (elastic modulus of 119 kPa, elongation at break of 451 % and breaking strength of 0.9 MPa) were sufficiently robust for practical operation.

In the compression test, all the hydrogels withstood 70 % compression deformation without breaking, with only a small amount of plastic deformation generated (Fig. 1F and G). All the double network hydrogels showed a compressive stress of about 0.9 MPa and a compression elastic modulus of about 130 kPa (Fig. 1F), which was 2 folds of that of the single network hydrogel (Fig. 1H). In addition, to test the fatigue resistance of hydrogels, the PAHT hydrogel was subjected to 20 cycles of tensile and compression tests (Fig. 1I and J) within the strain range of 0–100 % and 0–50 %, respectively. No obvious plastic deformation was observed, and the hysteresis loop was small. These results prove that, as expected [41], the double network hydrogel PAHT presented robust mechanical properties and will not break or fail in daily activities.

The hydrogel dressings are often designed to absorb the exudates in the wound environment [42]. However, excessive swelling will lead to the extreme expansion of the hydrogel volume and a sharp decline in its mechanical properties, which is not conducive to its continued protection of the wound [43]. In PBS at pH 7.4, the PAHT hydrogel rapidly absorbed medium, and then gradually achieved balance in the first 6 h.

The final swelling ratio was only 61.1 % (Fig. 2A). With this good swelling resistance, the fracture strength of PAHT hydrogel after swelling balance (0.57 MPa) was still larger than that of the PVA hydrogel (0.38 MPa) (Fig. 2B). On the other hand, the hydrogel dressings with maintained water content can offer a wet environment for wound healing [42]. Fig. 2C shows that the moisture contained in the PAHT hydrogel was gradually lost within 8 h, when no covering film was applied. However, in practical applications, the wound dressings are often covered with a protective film that resists contamination and retains moisture [44]. Therefore, the water loss rate would be significantly reduced, and is not a concern for our hydrogels to apply.

The functional components HBPL and TA in the hydrogel were physically loaded and could be released in the wound environment. When HBPL and TA existed alone, they achieved rapid release (Fig. 2D and E) with eventual releasing percentages of 88.1 % and 51.7 %, respectively. When HBPL and TA coexisted, the release of both HBPL and TA was slowed down with smaller percentages at the equilibrium state. The HBPL and TA are rich in positive charge and negative charge, respectively, and thereby the electrostatic interaction between HBPL and TA with the additional hydrogen bonding with the bulk molecules will then result in the slower release. It has to mention that in the *in vivo* application, the release of HBPL and TA would be much slower due to the less amount of medium compared with the *in vitro* experiments, thus much longer functioning is expected.

3.2. Antioxidant ability, antibacterial capacity and biocompatibility

Modulating the inflammatory response of the wound is essential to reduce the subsequent scar formation [7]. The presence of inflammation will lead to the increase of ROS along with the enhancement of oxidative stress, which further aggravates the inflammatory response [45]. DPPH is a kind of free radicals commonly used for antioxidant assay [46]. Due to the excellent antioxidant ability of TA, the PAT and PAHT hydrogels containing TA completely eliminated DPPH within 1 h (Fig. 2F). The PAH hydrogel containing only HBPL also had cleared 42.1 % radicals due to the reducibility of amino groups in HBPL. By contrast, the hydrogel matrix had no scavenging effect on DPPH. ROS *in vivo* mainly included ·OH, $\cdot O_2^-$ and H_2O_2, etc. For ·OH with the highest activity, even the hydrogel matrix exhibited a 63.3 % clearance, which was slightly smaller than the PAH hydrogel (65.4 %). The PAT and PATH had most efficiency with a value over 90 % (Fig. 2G). For the less active $\cdot O_2^-$ and H_2O_2, the hydrogel matrix and HBPL were not reactive, whereas the PAT and PATH showed efficient clearance as expected (Fig. 2H and I). In summary, the excellent antioxidant capacity of hydrogels was mainly attributed to the TA component, whereas was partially contributed by the HBPL when radicals exist.

Bacterial infection is an important cause of wound inflammation, hindering the wound healing and aggravating scar formation [9]. Considering the widespread emergence and spread of drug-resistant bacteria in recent years, MRSA and *E.coli* were used as the representatives of gram-positive and gram-negative bacteria respectively to test the antibacterial ability of hydrogels [47]. The surface contact method was used. Because the bacteria in the agar plate group multiplied to more than 100 times of the original number, the PA hydrogel without antibacterial ability (the number of bacteria should remain unchanged before and after contact) was used as the control group. As shown in Fig. 2J-L, the bacteria still survived after contacted with the PA hydrogel. After contacted with the PAT hydrogel, 50–80 % of bacteria were killed, which is consistent with the antibacterial ability of TA [31]. Almost all the bacteria were killed after contacted with the hydrogels

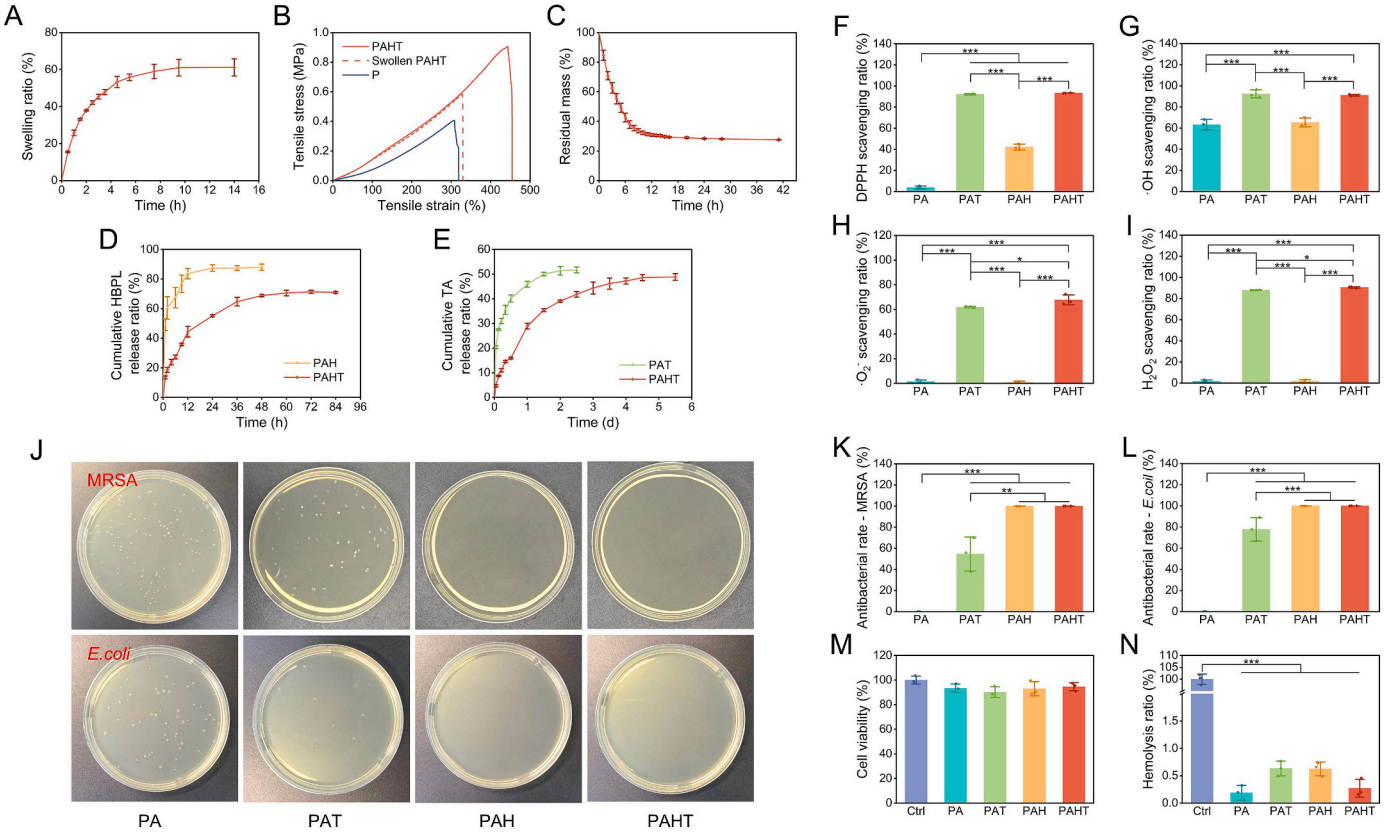

Fig. 2. Physiochemical and biological properties of hydrogels. (A) Swelling ability and (B) tensile property after swollen of PAHT hydrogel. (C) Moisturizing ability of PAHT hydrogel. Cumulative release of (D) HBPL and (E) TA. Scavenging capability of hydrogels to oxidants of (F) DPPH, (G)·OH, (H) $\cdot O_2^-$ and (I) H_2O_2. (J) Photographs of MRSA and *E.coli* colonies, and (K, L) corresponding quantitative calculation of antibacterial rates after treatments of different hydrogels. (M) Cell and (N) blood compatibility of hydrogels. n = 3, *P < 0.05, **P < 0.01 and ***P < 0.001.

containing HBPL, due to the destruction of bacterial cell membrane by a large number of positive amino groups in the cationic polymer HBPL [27]. Additionally, the molar ratio of TA in PAT to HBPL in PAH and PAHT was 2.35:1, indicating the relatively high antibacterial capacity of HBPL.

Wound dressings must be safe and harmless [48]. Therefore, the cytocompatibility and blood compatibility of hydrogels were analyzed [49]. The toxicity of different hydrogels to L929 cells was tested by the CCK-8 method. After 1 d of culture with the hydrogel extracts, all groups maintained more than 90 % cell viability compared with the Ctrl group (Fig. 2M). In the hemolysis analysis, the hemolysis ratios of all groups were below 1 % (Fig. 2N). These results demonstrate that our hydrogels possess good cellular and blood compatibility, and can be further studied *in vivo* without safety concern.

3.3. Healing of MRSA-infected wound in rats

To evaluate the efficacy of PAHT hydrogel dressing for the treatment of wounds *in vivo*, a rat model of full-thickness skin defect with MRSA infection was established (Fig. 3A). Fig. 3B and C shows that on day 3 the anti-infection ability of HBPL-containing hydrogels was obvious. The yellow pus caused by bacterial infection was observed in the Ctrl and PA groups without antibacterial ability. The suppuration of PAT group was reduced, representing decreased infection. The PAH and PAHT groups with HBPL had the best anti-infection effect and the cleanest wound surface. On day 12, the healing of PAHT group was the best, with almost complete closure of the wound. The quantitative statistics of wound healing (Fig. 3D) also shows the same conclusion. The healing speed of PAHT group was the fastest among 12 d, reaching a final wound closure of 98.0 %.

To further quantitatively analyze the *in vivo* anti-infection ability, the bacteria were isolated from the collected wound tissue, and cultured on an agar plate. Consistent with the macroscopic observation, a large number of bacteria were present in the wounds of Ctrl and PA groups, while the number of bacteria in the PAT group decreased. Most notably, the bacterial contents of PAH and PAHT groups with better antibacterial function were reduced by more than one order of magnitude (Fig. 3 E and F).

Elisa results reveal that the expressions of pro-inflammatory factors tumor necrosis factor-α (TNF-α), Interleukin-1β (IL-1β) and IL-6 were down-regulated in all the treatment groups, and the down-regulation was most obvious in the PAHT group with the strongest antibacterial and antioxidant function (Fig. 4A–C). Correspondingly, the anti-inflammatory factors IL-4 and IL-10 were upregulated in all the treatment groups, especially in the PAHT group (Fig. 4D and E). These results suggest that our hydrogel dressings, especially the PAHT hydrogel, laid significant efficacy on anti-infection, anti-inflammatory and pro-healing *in vivo*.

The pathological staining was performed to facilitate a more detailed analysis of wound healing. Fig. 4F reveals the tissue regeneration, inflammatory infiltration, and collagen deposition throughout the healing process. In the H&E staining, on day 6, consistent with the Elisa results, a massive infiltration of inflammatory cells was observed in the Ctrl and PA groups, whereas their number was reduced in the PAT hydrogel group. The level of inflammation in the PAH and PAHT groups was the lowest, suggesting the antibacterial property takes more important role in reducing the inflammation of infected wounds. The wound width was significantly reduced on day 12. Notably, the wounds in the PAHT group were basically completely healed, which was consistent with the macroscopic photographic results. In addition, on day 12, the new epithelium in the PAH and PAHT groups was obviously thicker and more complete than in the other groups, and the appendages such as hair

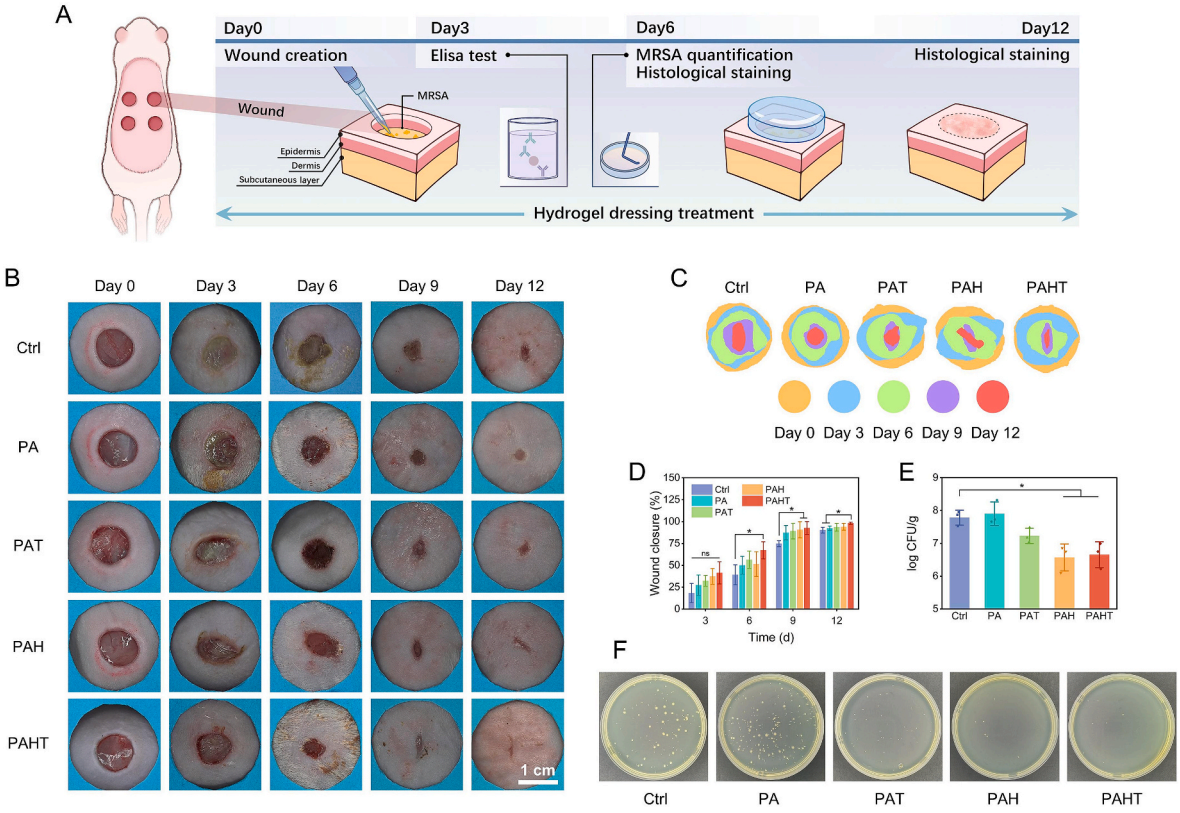

Fig. 3. Hydrogels accelerated wound closure and killed bacteria in MRSA-infected full-thickness skin defects in rats. (A) Scheme of the wound healing experiment. (B) Representative images of infected wounds treated with different hydrogels at different periods. (C) Diagram of the dynamic wound healing process, and (D) quantitative analysis of wound area (n = 3) within 12 d for each treatment. (E) Quantitative calculation of MRSA colonies in wounds after treatment with different hydrogels, and (F) corresponding photos. n = 3, *P < 0.05, **P < 0.01 and ***P < 0.001.

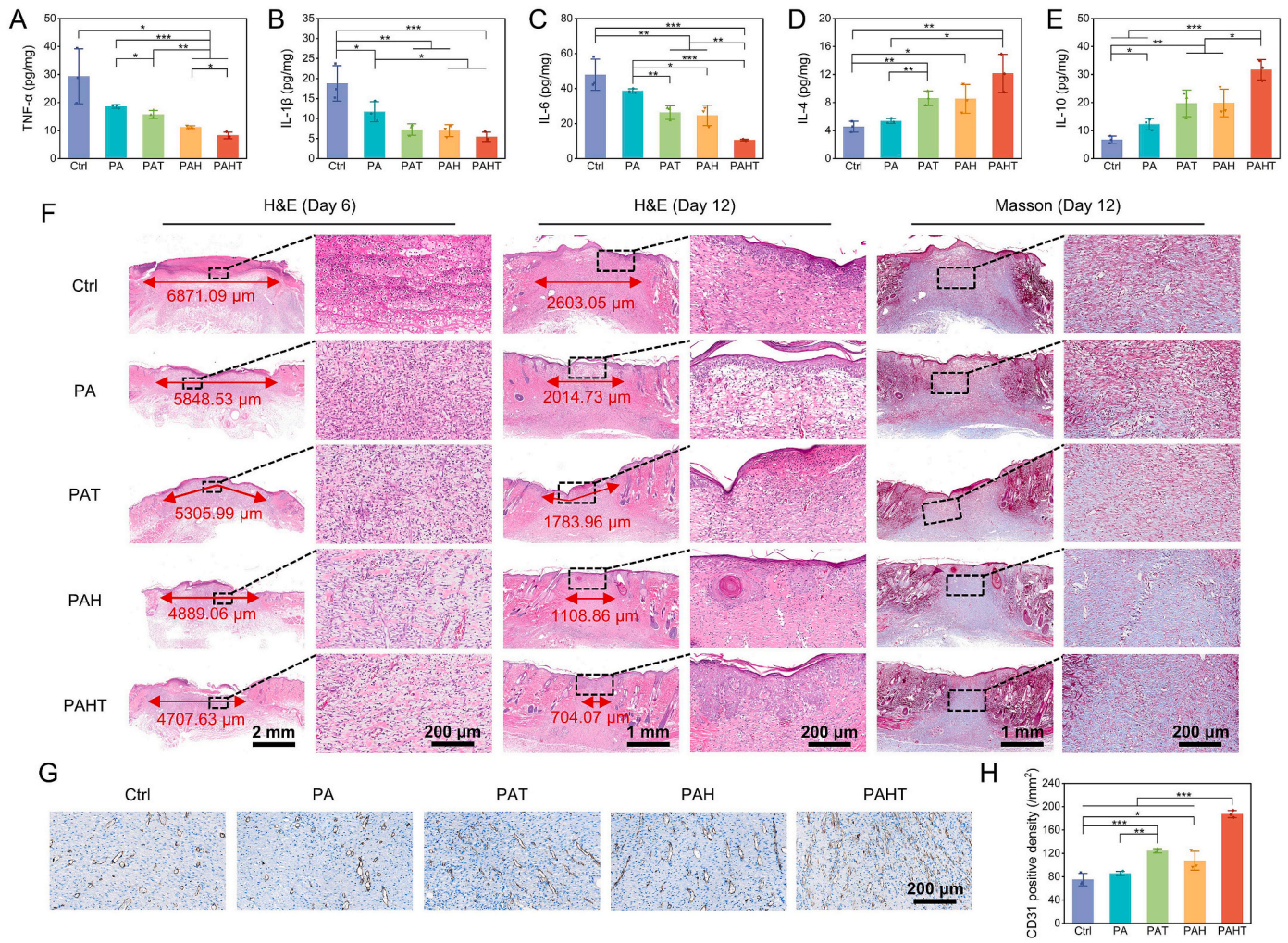

Fig. 4. Elisa and histological analysis of wound tissues in rats. Expression levels of (A) TNF-α, (B) IL-1β, (C) IL-6, (D) IL-4 and (E) IL-10 inflammatory factors in wounds. (F) H&E and Masson staining during the wound healing process. (G) CD31 immunohistochemical staining of wound tissue at day 12, and (H) quantitative analysis. n = 3, *P < 0.05, **P < 0.01 and ***P < 0.001.

follicles began to appear. Meanwhile, the Masson staining manifests that the PAT, and especially the PAH and PAHT groups exhibited denser and more abundant collagen deposition. It is known that angiogenesis plays an important role in wound healing, while CD31 can represent formation of new blood vessels [50]. Immunohistochemical staining of CD31 and corresponding quantitative analysis results indicate that the PAHT hydrogel treatment significantly increased the expression of CD31 (Fig. 4G and H). These results reveal that our antibacterial and antioxidant dressing held a strong positive effect in accelerating wound closure and epidermal regeneration, promoting collagen deposition and angiogenesis, thus providing powerful support for skin wound recovery.

3.4. Suppression of MRSA-infected hypertrophic scars in rabbits

Because the rat model could not form excessive scar hyperplasia, we built a rabbit ear hypertrophic scar model that is similar to human [51]. The MRSA infection was further implemented to simulate the infection prone to occur in life. We used this model to study the ability of our hydrogel dressings to inhibit scar formation. After the wounds were made, the hydrogel dressings were applied for treatment until the wounds healed completely 4 w later (Fig. 5A), and then another 4 w culture was maintained to stabilize the scar development. The imaging tracking of wound healing and scar development stages was performed in this model (Fig. 5B). The wound healing stage in the first 4 w was basically consistent with the results of the rat model. At the end of week 4, prominent red scars were clearly observed in the Ctrl, PA, and PAT groups. Afterwards, the scars were gradually stabilized, and their color faded along with time prolongation. Among all the groups, the scars in the PAH and PAHT groups had the closest appearance to normal skin.

Similarly, histological analyses were used to monitor the scar formation process (Fig. 6A). On the one hand, the H&E staining visually displayed the thickness of scars. The average thickness of Ctrl group without hydrogel treatment was 936.0 μm, exceedingly twice the thickness of normal skin (357.2 μm). The non-functional hydrogel PA had no obvious inhibitory effect on the scar thickness. Along with the enrichment of the hydrogel function from PAT, PAH to PAHT, the scar thickness gradually decreased. The average scar thickness in the PAHT group was 592.5 μm. Compared with the Ctrl group, it decreased by 36.7 % (Fig. 6B). However, due to individual difference, the healthy skin thickness varies among rabbits, and thus the simple comparison of scar thickness was not rigorous enough [52]. Therefore, SEI, the ratio of scar area to normal area was calculated [53], which shared the same trend as that of the thickness. The PAHT group possessed the lowest SEI value (1.45), representing the lowest degree of scar bulge (Fig. 6C). On the other hand, the formation of hypertrophic scars is closely related to the excessive deposition of collagen fibers [2]. The CVF calculated from the Masson staining (Fig. 6D) embodies that the untreated Ctrl group showed the maximum value of 63.1 %, while the PAHT group (45.4 %) was closest to the normal level (38.7 %), indicating that the excessive deposition of collagen was significantly inhibited [21].

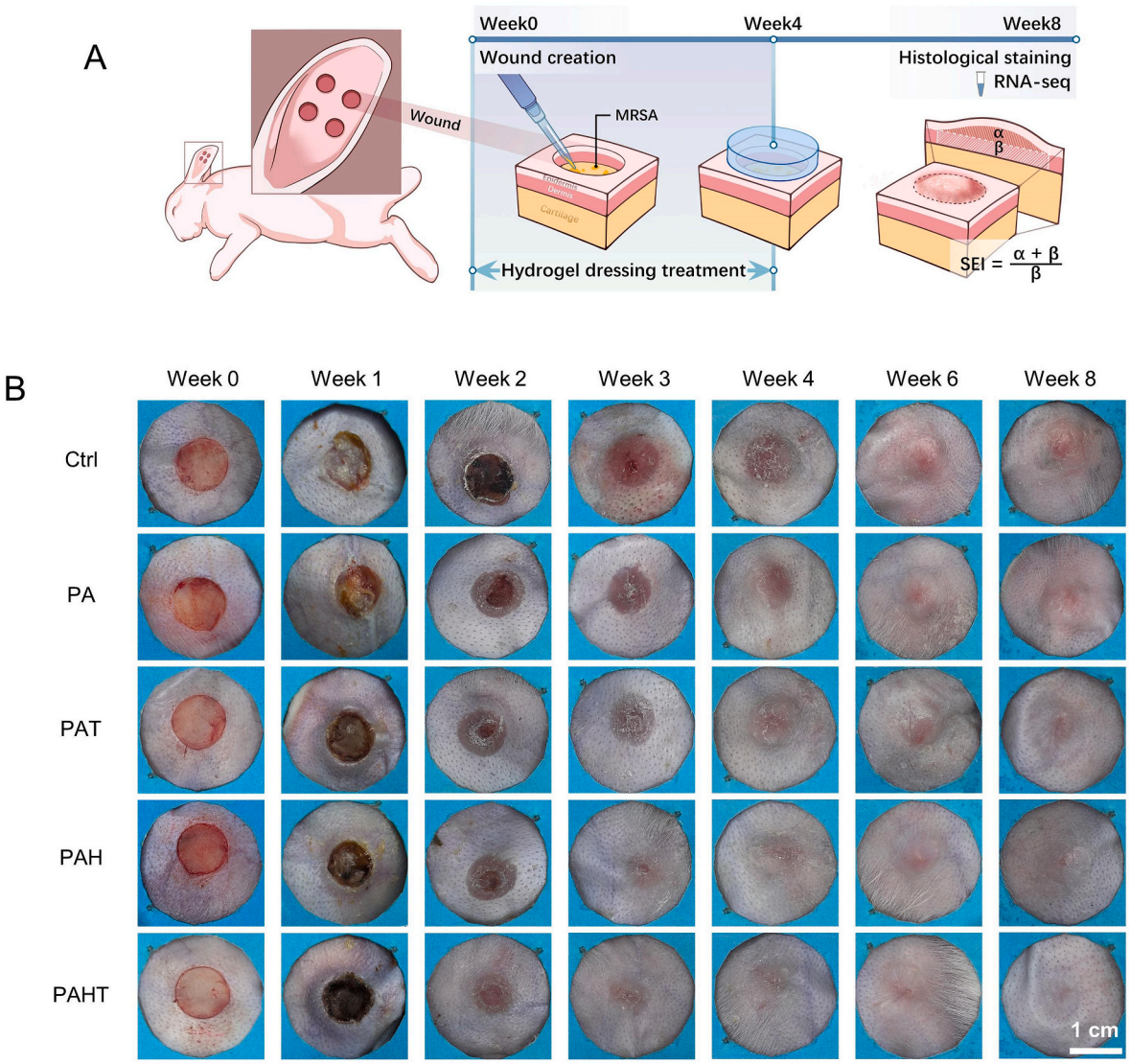

Fig. 5. Hydrogels suppressed hypertrophic scar formation in MRSA-infected wounds in rabbit ears. (A) Scheme of the hypertrophic scar experiment. (B) Representative images of wound closure and subsequent scar formation and stabilization being treated with different hydrogels at different periods.

Moreover, the type of collagen fibers affects skin morphology crucially. The thick and hard type I collagen is the framework, which is usually highly expressed in the hypertrophic scars, causing skin stiff. By contrast, the smaller type III collagen renders softness and elasticity to skin, with low expression in the hypertrophic scars [54]. The type I (orange) and type III (green) collagen were distinguished using polarized light to observe the Sirius red staining (Fig. 6A). There was almost no type III collagen in the Ctrl group. After treatment with the functional hydrogels, the proportion of type III collagen increased. In addition, the excessive activity of myofibroblasts will lead to scar formation and further contracture. α-Smooth muscle actin (α-SMA), as the marker for the transformation of fibroblasts into myofibroblasts, is specifically overexpressed in hypertrophic scars [55]. Therefore, the content of α-SMA of different groups was observed by immunofluorescence staining (Fig. 6A). In the Ctrl group, the α-SMA expression was particularly obvious. With the enrichment of hydrogel functions, the expression of α-SMA gradually decreased, and the status of the PAHT group was closest to that of the normal skin. In summary, the PAHT, an antibacterial and antioxidant hydrogel dressing, fulfilled a vital inhibitory role in the formation of hypertrophic scars.

The RNA sequencing (RNA seq) experiment was then conducted to explore the underlying mechanism of PAHT hydrogel in accelerating the healing of infected wounds and inhibiting the generation of hypertrophic scars. Principal component analysis (PCA) of Norm, Ctrl, and PAHT groups showed significant differences in transcriptome profiles. Compared with the Ctrl group, the PAHT group was closer to the Norm group (Fig. 7A). In the volcanic map, the Ctrl vs Norm displayed 1286 upregulated genes and 1061 downregulated genes (Fig. 7B), while the PAHT vs Ctrl showed 713 upregulated genes and 876 downregulated genes (Fig. 7C). The gene heatmap manifests that compared to the Norm group, the genes related to immune and inflammatory responses such as C–C motif chemotherapy light 19 (CCL19), defensin beta 1 (DEFB1), CD4 molecule (CD4), interleukin 1 alpha (IL1A), and lymphotoxin beta (LTB) were significantly upregulated in the Ctrl group (Fig. 7D). After the PAHT hydrogel treatment, the expression of these genes returned to the levels close to those of the Norm group. The genes upregulated in the Ctrl vs Norm and downregulated in the PAHT vs Ctrl were collected, and the potential signaling pathways were analyzed by Kyoto Encyclopedia of Genes and Genomes (KEGG). It turned out that differentially expressed genes were significantly involved in the *Staphylococcus aureus* infection, Th1 and Th2 cell differentiation, Th17 cell differentiation, and NF kappa B signaling pathway related to host defense, immune regulation, and inflammatory pathways (Fig. 7E). In conclusion, the PAHT hydrogel promoted tissue repair and reduced scar formation via

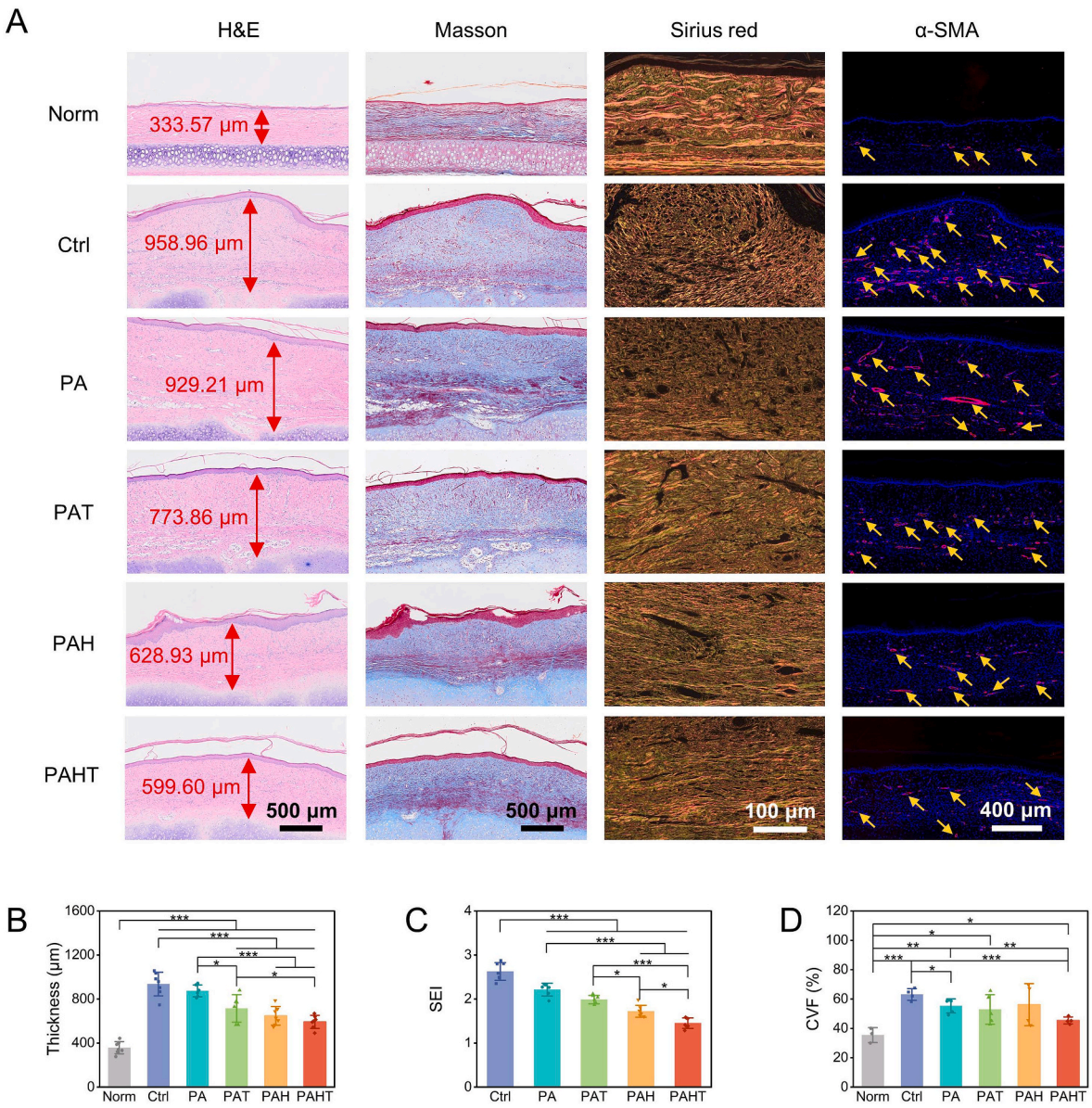

Fig. 6. Histological analysis of scar tissues in rabbit ears. (A) H&E staining, Masson staining, Sirius red staining (polarized light observation) and α-SMA immunofluorescence staining for each group. Quantitative analysis of (B) thickness and (C) SEI in H&E staining (n = 6), and (D) CVF in Masson staining (n = 4). *P < 0.05, **P < 0.01 and ***P < 0.001.

reducing infection and controlling inflammation.

To prevent scar formation, corresponding measures can be taken according to the different stages of wound healing. During the inflammatory phase, therapies alleviating inflammation should be used [21], which is the fundamental basis of our design. HBPL and TA loaded in the PAHT hydrogel could kill bacteria as well as reduce oxidative stress, thus the inflammation was best controlled and HSs were least produced. The PAH and PAT hydrogels also had good anti-scar ability. Our study demonstrated that in the infected wounds, controlling the bacterial infection had a better anti-scar effect than reducing the oxidative stress. By contrast, the PA hydrogel had limited effect on inhibiting scar formation because it could only provide physical protection and retain water. Since few other anti-scar materials have been reported to target bacterial infections, our PAHT hydrogel dressing is highly competitive.

So far most of the antibacterial dressings contain the bactericidal components that are toxic to cells and tissues. For example, the tannic acid-Fe complex was used to achieve antibacterial function through photothermal effect and photodynamic effect [56,57]. The high temperature, overaccumulation of ferric ions, and generated free radicals may cause uncontrolled toxicity. The use of near-infrared laser causes high cost too. Moreover, very few dressings have been investigated with respect to the inhibition of scar formation. Indeed, it is still a big change to prepare wound dressings with superior antibacterial and scar-inhibiting performance, non-toxicity to cells and tissues, and lower cost. Compared with those previous studies, our hydrogel could be facilely fabricated with low cost and mass producibility, while they were very effective in bactericidal and scar inhibition. Due to their nontoxic components, the hydrogel had excellent biocompatibility without noticeable toxicity.

4. Conclusion

A double networking hydrogel PAHT was obtained by using PVA and agarose, which was further loaded with HBPL and TA to achieve antibacterial and antioxidant functions for promoting wound healing, and more importantly inhibiting scar developing. The preparation process of

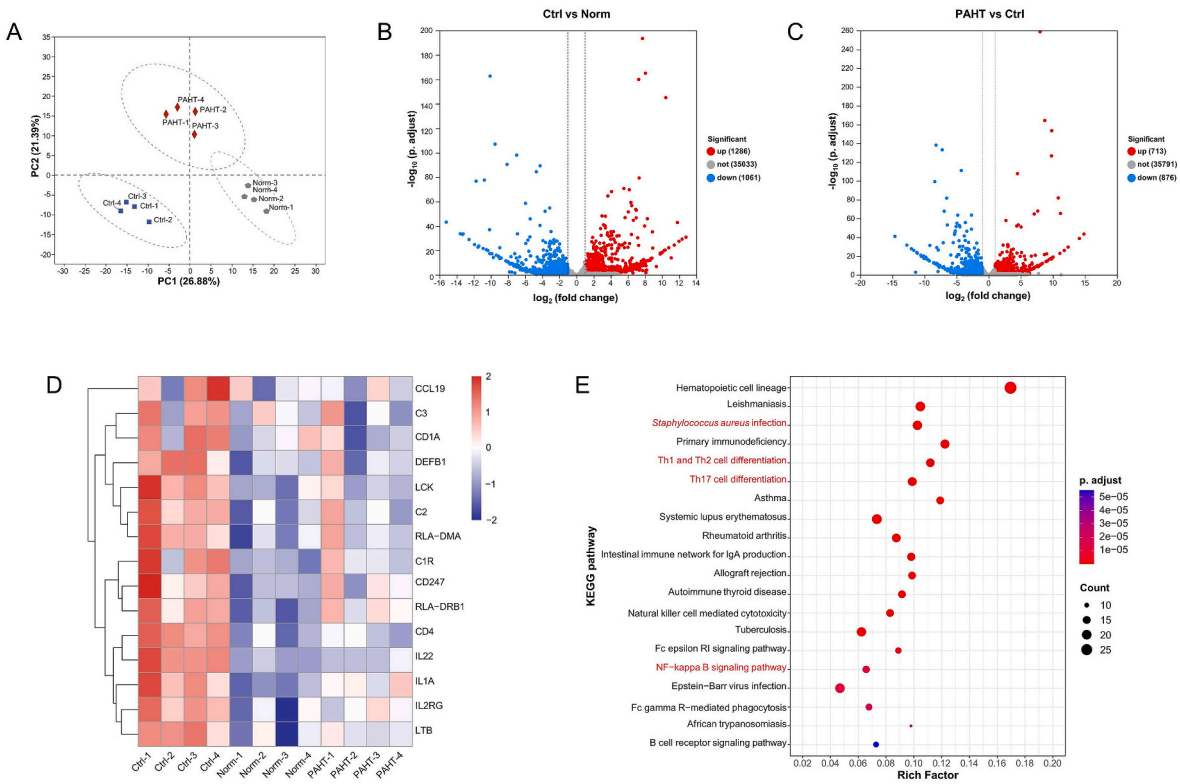

Fig. 7. Mechanistic analysis of PAHT hydrogel suppressing hypertrophic scar formation in rabbit ears. (A) PCA of Normal (Norm), Ctrl, and PAHT groups. Differently expressed genes of (B) Ctrl vs Norm, and (C) PAHT vs Ctrl presented in volcano plots. The threshold of $\log_2$ (fold change) was 1. (D) Heatmap analysis of differentially expressed genes. (E) Enriched KEGG pathways of genes upregulated in Ctrl vs Norm, and downregulated in PAHT vs Ctrl.

hydrogel was simple and easy to repeat, and the raw materials related were safe, inexpensive and widely used. Besides, the excellent strength, toughness and fatigue resistance had been verified through mechanical experiments, proving the validity of double network structure. The hydrogel demonstrated an efficient killing ability against Gram-negative and Gram-positive bacteria, and was able to quickly remove ROS such as ·OH, $\cdot O_2^-$, and H_2O_2. In the rat model, the PAHT hydrogel displayed the ability to promote wound healing, kill bacteria *in vivo*, reduce inflammation, and promote tissue regeneration. In the rabbit model, the PAHT dressing showed a significant effect on suppressing HSs formation. Specifically, the PAHT hydrogel was able to reduce scar thickness, reduce collagen deposition, regulate collagen type and down-regulate α-SMA production. RNA-seq analysis demonstrates that the promising effect of PAHT hydrogel mainly caused by its ability to efficiently resist MRSA and thus alleviate inflammatory reactions. In summary, the PAHT hydrogel presents a broad translational prospect, and will play a key role in the field of anti-scarring of infected wounds.

Data availability

The raw/processed data required to reproduce these findings are available from the corresponding author upon reasonable request.

Ethics approval and consent to participate

The rat experiments were approved by the Experimental Animal Ethics Committee of Hangzhou Medical College following the Institutional Guidelines (ZJCLA-IACUC-20010294), and the rabbit experiments were approved by the Experimental Animal Ethics Committee of Hangzhou Medical College following the Institutional Guidelines (ZJCLA-IACUC-20010315). All animal experiments were performed in accordance with relevant ethical regulations.

CRediT authorship contribution statement

Xiaoqing Liu: Writing – review & editing, Writing – original draft, Visualization, Validation, Methodology, Investigation, Formal analysis, Data curation, Conceptualization. **Yiming Sun:** Writing – review & editing, Writing – original draft, Visualization, Validation, Methodology, Investigation, Formal analysis, Data curation, Conceptualization. **Jie Wang:** Methodology, Investigation. **Yongyuan Kang:** Methodology, Investigation. **Zhaolong Wang:** Investigation. **Wangbei Cao:** Methodology. **Juan Ye:** Writing – review & editing, Supervision, Resources, Conceptualization. **Changyou Gao:** Writing – review & editing, Supervision, Resources, Project administration, Funding acquisition, Conceptualization.

Declaration of competing interest

The authors declare that they have no known competing financial interests or personal relationships that could have appeared to influence the work reported in this paper.

Acknowledgments

This work was supported by the Shanxi-Zheda Institute of Advanced Materials and Chemical Engineering (2021SZ-TD004), the Natural Science Foundation of Zhejiang Province (LD21E030001), the Joint Fund of National Natural Science Foundation of China (U22A20155), and the Lingyan Program of Zhejiang Province (2022C01106).

References

[1] H.J. Lee, Y.J. Jang, Recent Understandings of biology, prophylaxis and treatment strategies for hypertrophic scars and keloids, Int. J. Mol. Sci. 19 (2018) 711, https://doi.org/10.3390/ijms19030711.

[2] M. Xue, C.J. Jackson, Extracellular matrix reorganization during wound healing and its impact on abnormal scarring, Adv. Wound Care 4 (2015) 119–136, https://doi.org/10.1089/wound.2013.0485.
[3] T. Zhang, X.F. Wang, Z.C. Wang, et al., Current potential therapeutic strategies targeting the TGF-β/Smad signaling pathway to attenuate keloid and hypertrophic scar formation, Biomed. Pharmacother. 129 (2020), 110287, https://doi.org/10.1016/j.biopha.2020.110287.
[4] L. Moretti, J. Stalfort, T.H. Barker, et al., The interplay of fibroblasts, the extracellular matrix, and inflammation in scar formation, J. Biol. Chem. 298 (2022), 101530, https://doi.org/10.1016/j.jbc.2021.101530.
[5] B. Brian, M. Andrea, R. Brian, Keloids and hypertrophic scars: pathophysiology, classification, and treatment, Dermatol. Surg. 43 (2017) 3–18, https://doi.org/10.1097/DSS.0000000000000819.
[6] C.C. Finnerty, M.G. Jeschke, L.K. Branski, et al., Hypertrophic scarring: the greatest unmet challenge after burn injury, Lancet 388 (2016) 1427–1436, https://doi.org/10.1016/S0140-6736(16)31406-4.
[7] R. Ogawa, Keloid and hypertrophic scars are the result of chronic inflammation in the reticular dermis, Int. J. Mol. Sci. 18 (2017) 606, https://doi.org/10.3390/ijms18030606.
[8] Y. Liang, J. He, B. Guo, Functional hydrogels as wound dressing to enhance wound healing, ACS Nano 15 (2021) 12687–12722, https://doi.org/10.1021/acsnano.1c04206.
[9] Y. Yang, Y. Liang, J. Chen, et al., Mussel-inspired adhesive antioxidant antibacterial hemostatic composite hydrogel wound dressing via photo-polymerization for infected skin wound healing, Bioact. Mater. 8 (2022) 341–354, https://doi.org/10.1016/j.bioactmat.2021.06.014.
[10] N.A. Turner, B.K. Sharma-Kuinkel, S.A. Maskarinec, et al., Methicillin-resistant Staphylococcus aureus: an overview of basic and clinical research, Nat. Rev. Microbiol. 17 (2019) 203–218, https://doi.org/10.1038/s41579-018-0147-4.
[11] M.F. Mohamed, A. Abdelkhalek, M.N. Seleem, Evaluation of short synthetic antimicrobial peptides for treatment of drug-resistant and intracellular Staphylococcus aureus, Sci. Rep. 6 (2016), 29707, https://doi.org/10.1038/srep29707.
[12] L. Sethuram, J. Thomas, Therapeutic applications of electrospun nanofibers impregnated with various biological macromolecules for effective wound healing strategy - a review, Biomed. Pharmacother. 157 (2023), 113996, https://doi.org/10.1016/j.biopha.2022.113996.
[13] I. Negut, V. Grumezescu, A.M. Grumezescu, Treatment strategies for infected wounds, Molecules 23 (2018) 2392, https://doi.org/10.3390/molecules23092392.
[14] R. Ogawa, The most current algorithms for the treatment and prevention of hypertrophic scars and keloids: a 2020 update of the algorithms published 10 years ago, Plast. Reconstr. Surg. 149 (2022) 79–94, https://doi.org/10.1097/PRS.0000000000008667.
[15] H. Zhang, M. Guo, T. Zhu, et al., A careob-like nanofibers with a sustained drug release profile for promoting skin wound repair and inhibiting hypertrophic scar, Composites, Part B 236 (2022), 109790, https://doi.org/10.1016/j.compositesb.2022.109790.
[16] K. Wu, M. Fu, Y. Zhao, et al., Anti-oxidant anti-inflammatory and antibacterial tannin-crosslinked citrate-based mussel-inspired bioadhesives facilitate scarless wound healing, Bioact. Mater. 20 (2023) 93–110, https://doi.org/10.1016/j.bioactmat.2022.05.017.
[17] S. Wu, Y. Yang, S. Wang, et al., Dextran and peptide-based pH-sensitive hydrogel boosts healing process in multidrug-resistant bacteria-infected wounds, Carbohydrate Polymers 278 (2022), 118994, https://doi.org/10.1016/j.carbpol.2021.118994.
[18] J. Zhang, Y. Zheng, J. Lee, et al., A pulsatile release platform based on photo-induced imine-crosslinking hydrogel promotes scarless wound healing, Nat. Commun. 12 (2021) 1670, https://doi.org/10.1038/s41467-021-21964-0.
[19] W. Weng, S. He, H. Song, et al., Aligned carbon nanotubes reduce hypertrophic scar via regulating cell behavior, ACS Nano 12 (2018) 7601–7612, https://doi.org/10.1021/acsnano.7b07439.
[20] Y. Zhang, S. Wang, Y. Yang, et al., Scarless wound healing programmed by core-shell microneedles, Nat. Commun. 14 (2023) 3431, https://doi.org/10.1038/s41467-023-39129-6.
[21] J.J. Hu, M. Wang, X.X. Lei, et al., Scarless healing of injured vocal folds using an injectable hyaluronic acid-waterborne polyurethane hybrid hydrogel to tune inflammation and collagen deposition, ACS Appl. Mater. Interfaces 14 (2022), https://doi.org/10.1021/acsami.2c07225, 42827−42840.
[22] Y. Shen, G. Xu, H. Huang, et al., Sequential release of small extracellular vesicles from bilayered thiolated alginate/polyethylene glycol diacrylate hydrogels for scarless wound healing, ACS Nano 15 (2021) 6352–6368, https://doi.org/10.1021/acsnano.0c07714.
[23] Q. Zhang, L. Shi, H. He, et al., Down-regulating scar formation by microneedles directly via a mechanical communication pathway, ACS Nano 16 (2022) 10163–10178, https://doi.org/10.1021/acsnano.1c11016.
[24] B. Zhao, W. Guo, X. Zhou, et al., Ferroptosis-mediated synergistic therapy of hypertrophic scarring based on metal-organic framework microneedle patch, Adv. Funct. Mater. 33 (2023), 2300575, https://doi.org/10.1002/adfm.202300575.
[25] W. Cao, X. Zhou, C. Tu, et al., A broad-spectrum antibacterial and tough hydrogel dressing accelerates healing of infected wound in vivo, Biomater. Adv. 145 (2023), 213244, https://doi.org/10.1016/j.bioadv.2022.213244.
[26] M.A.M. Jahromi, P.S. Zangabad, S.M.M. Basri, et al., Nanomedicine and advanced technologies for burns: preventing infection and facilitating wound healing, Adv. Drug Deliv. Rev. 123 (2018) 33–64, https://doi.org/10.1016/j.addr.2017.08.001.
[27] Z. Yang, Y. Xi, J. Bai, et al., Covalent grafting of hyperbranched poly-L-lysine on Ti-based implants achieves dual functions of antibacteria and promoted osteointegration in vivo, Biomaterials 269 (2021), 120534, https://doi.org/10.1016/j.biomaterials.2020.120534.
[28] H. Lu, C. Tu, T. Zhou, et al., A ROS-scavenging hydrogel loaded with bacterial quorum sensing inhibitor hyperbranched poly-L-lysine promotes the wound scar-free healing of infected skin in vivo, Chem. Eng. J. 436 (2022), 135130, https://doi.org/10.1016/j.cej.2022.135130.
[29] C. Tu, H. Lu, T. Zhou, et al., Promoting the healing of infected diabetic wound by an anti-bacterial and nano-enzyme-containing hydrogel with inflammation-suppressing, ROS-scavenging, oxygen and nitric oxide-generating properties, Biomaterials 286 (2022), 121597, https://doi.org/10.1016/j.biomaterials.2022.121597.
[30] H. Lei, D. Fan, Conductive, adaptive, multifunctional hydrogel combined with electrical stimulation for deep wound repair, Chem. Eng. J. 421 (2021), 129578, https://doi.org/10.1016/j.cej.2021.129578.
[31] C. Cao, N. Yang, Y. Zhao, et al., Biodegradable hydrogel with thermo-response and hemostatic effect for photothermal enhanced anti-infective therapy, Nano Today 39 (2021), 101165, https://doi.org/10.1016/j.nantod.2021.101165.
[32] R. Xu, S. Ma, P. Lin, et al., High strength astringent hydrogels using protein as the building block for physically cross-linked multi-network, ACS Appl. Mater. Interfaces 10 (2018) 7593–7601, https://doi.org/10.1021/acsami.7b04290.
[33] W. Ge, S. Cao, F. Shen, et al., Rapid self-healing, stretchable, moldable, antioxidant and antibacterial tannic acid-cellulose nanofibril composite hydrogels, Carbohydrate Polymers 224 (2019), 115147, https://doi.org/10.1016/j.carbpol.2019.115147.
[34] E.A. Kamoun, E.S. Kenawy, X. Chen, A review on polymeric hydrogel membranes for wound dressing applications: PVA-based hydrogel dressings, J. Adv. Res. 8 (2017) 217–233, https://doi.org/10.1016/j.jare.2017.01.005.
[35] S. Wu, M. Hua, Y. Alsaid, et al., Poly(vinyl alcohol) hydrogels with broad-range tunable mechanical properties via the hofmeister effect, Adv. Mater. 33 (2021), 2007829, https://doi.org/10.1002/adma.202007829.
[36] H. Zhang, N. Tang, X. Yu, et al., Strong and tough physical eutectogels regulated by the spatiotemporal expression of non-covalent interactions, Adv. Funct. Mater. 32 (2022), 2206305, https://doi.org/10.1002/adfm.202206305.
[37] M. Hua, S. Wu, Y. Ma, et al., Strong tough hydrogels via the synergy of freeze-casting and salting out, Nature 590 (2021) 594–599, https://doi.org/10.1038/s41586-021-03212-z.
[38] J. Yang, K. Li, C. Tang, Recent progress in double network elastomers: one plus one is greater than two, Adv. Funct. Mater. 32 (2022), 2110244, https://doi.org/10.1002/adfm.202110244.
[39] J. Bai, X. Zuo, X. Feng, et al., Dynamic titania nanotube surface achieves UV-triggered charge reversal and enhances cell differentiation, ACS Appl. Mater. Interfaces 11 (2019) 36939–36948, https://doi.org/10.1021/acsami.9b11536.
[40] L. Han, X. Lu, K. Liu, Mussel-inspired adhesive and tough hydrogel based on nanoclay confined dopamine polymerization, ACS Nano 11 (2017) 2561–2574, https://doi.org/10.1021/acsnano.6b05318.
[41] J.P. Gong, Y. Katsuyama, T. Kurokawa, et al., Double-network hydrogels with extremely high mechanical strength, Adv. Mater. 15 (2003) 1155–1158, https://doi.org/10.1002/adma.200304907.
[42] M.H. Norahan, S.C. Pedroza-González, M.G. Sánchez-Salazar, et al., Structural and biological engineering of 3D hydrogels for wound healing, Bioact. Mater. 24 (2023) 197–235, https://doi.org/10.1016/j.bioactmat.2022.11.019.
[43] C. Wei, P. Tang, Y. Tang, Sponge-like macroporous hydrogel with antibacterial and ROS scavenging capabilities for diabetic wound regeneration, Adv. Healthcare Mater. 11 (2022), 2200717, https://doi.org/10.1002/adhm.202200717.
[44] H.M. Nguyen, T.T.N. Le, A.T. Nguyen, et al., Biomedical materials for wound dressing: recent advances and applications, RSC Adv. 13 (2023) 5509–5528, https://doi.org/10.1039/d2ra07673j.
[45] X. Qiu, Y. Yu, H. Liu, et al., Remodeling the periodontitis microenvironment for osteogenesis by using a reactive oxygen species-cleavable nanoplatform, Acta Biomater. 135 (2021) 593–605, https://doi.org/10.1016/j.actbio.2021.08.009.
[46] M.C. Foti, Use and Abuse of the DPPH$^{\bullet}$ radical, J. Agric. Food Chem. 63 (2015) 8765–8776, https://doi.org/10.1021/acs.jafc.5b03839.
[47] Y. Liang, B. Chen, M. Li, et al., Injectable antimicrobial conductive hydrogels for wound disinfection and infectious wound healing, Biomacromolecules 21 (2020) 1841–1852, https://doi.org/10.1021/acs.biomac.9b01732.
[48] W. Peng, D. Li, K. Dai, et al., Recent progress of collagen, chitosan, alginate and other hydrogels in skin repair and wound dressing applications, Int. J. Biol. Macromol. 208 (2022) 400–408, https://doi.org/10.1016/j.ijbiomac.2022.03.002.
[49] L. Deng, H. Lu, C. Tu, et al., A tough synthetic hydrogel with excellent post-loading of drugs for promoting the healing of infected wounds in vivo, Biomater. Adv. 134 (2022), 112577, https://doi.org/10.1016/j.msec.2021.112577.
[50] W. Cao, S. Peng, Y. Yao, et al., A nanofibrous membrane loaded with doxycycline and printed with conductive hydrogel strips promotes diabetic wound healing in vivo, Acta Biomater. 152 (2022) 60–73, https://doi.org/10.1016/j.actbio.2022.08.048.
[51] O. Kloeters, A. Tandara, T.A. Mustoe, Hypertrophic scar model in the rabbit ear: a reproducible model for studying scar tissue behavior with new observations on silicone gel sheeting for scar reduction, Wound Repair Regen. 15 (2007) S40–S45, https://doi.org/10.1111/j.1524-475X.2007.00224.x.
[52] D.E. Morris, M. D, M. Wu, et al., Acute and chronic animal models for excessive dermal scarring: quantitative studies, Plast. Reconstr. Surg. 100 (1997) 674–681, https://doi.org/10.1097/00006534-199709000-00021.
[53] O. Kloeters, A. Tandara, T.A. Mustoe, Hypertrophic scar model in the rabbit ear: a reproducible model for studying scar tissue behavior with new observations on silicone gel sheeting for scar reduction, Wound Repair Regen. 15 (2007) S40–S45, https://doi.org/10.1111/j.1524-475X.2007.00224.x.

[54] H. Kim, H. Im, H. Chang, et al., Correlation between collagen type I/III ratio and scar formation in patients undergoing immediate reconstruction with the round block technique after breast-conserving surgery, Biomedicines 11 (2023) 1089, https://doi.org/10.3390/biomedicines11041089.

[55] J.Q. Coentro, E. Pugliese, G. Hanley, et al., Current and upcoming therapies to modulate skin scarring and fibrosis, Adv. Drug Deliv. Rev. 146 (2019) 37–59, https://doi.org/10.1016/j.addr.2018.08.009.

[56] W. Guo, Y. Li, C. Zhu, et al., Tannic acid-Fe^{3+} dual catalysis induced rapid polymerization of injectable poly(lysine) hydrogel for infected wound healing, Int. J. Biol. Macromol. 294 (2023), 125911, https://doi.org/10.1016/j.ijbiomac.2023.125911.

[57] S. Bochani, A. Zarepour, A. Kalantari-Hesari, et al., Injectable, antibacterial, and oxygen-releasing chitosan-based hydrogel for multimodal healing of bacteria-infected wounds, J. Mater. Chem. B 11 (2023) 8056–8068, https://doi.org/10.1039/d3tb01278f.